Journal of The Electrochemical Society, 2024 **171** 120523

Visualising the Effect of Areal Current Density on the Performance and Degradation of Lithium Sulfur Batteries Using Operando Optical Microscopy

Rhodri E. Owen,[1,2,3,z] Wenjia Du,[3,4] Jason Millichamp,[1,2] Paul R. Shearing,[3,4] Dan J. L. Brett,[5] and James B. Robinson[1,2,3,z]

[1]*Advanced Propulsion Lab, Marshgate, University College London, London, E20 2AE, United Kingdom*
[2]*Electrochemical Innovation Laboratory, University College London, Torrington Place, London WC1E 7JE, United Kingdom*
[3]*The Faraday Institution, Quad One, Becquerel Avenue, Harwell Science and Innovation Campus, Didcot, OX11 0RA, United Kingdom*
[4]*ZERO Institute, University of Oxford, Osney Mead, Oxford, OX2 0ES, United Kingdom*
[5]*Prosemino Ltd., London SE16 7LG, United Kingdom*

The degradation of lithium sulfur (Li-S) batteries poses significant challenges to their commercial viability and occurs largely due to the complex electrochemical reactions and structural transformations that take place during charge-discharge cycles. This study employs optical microscopy techniques to investigate and quantify the degradation mechanisms in Li-S batteries. By capturing high-resolution, time-lapsed images of both electrodes and the electrolyte-filled interelectrode space, key morphological changes can be identified and analysed, such as the formation and growth of lithium dendrites, sulfur dissolution, and electrode-electrolyte interface degradation. Quantitative image analysis is conducted to measure the extent of these changes, providing insights into their impact on battery performance. Our findings reveal critical correlations between specific morphological features and electrochemical inefficiencies, contributing to a deeper understanding of the degradation pathways in Li-S batteries. This optical microscopy approach offers a non-destructive, cost-effective, real-time method to monitor battery health, potentially guiding the development of more durable and efficient Li-S batteries.

 [DOI: 10.1149/1945-7111/ad9cc6]

Manuscript submitted August 13, 2024; revised manuscript received October 31, 2024. Published December 18, 2024.

With the effects of global warming becoming significantly more prevalent, it is essential to rapidly move away from carbon dioxide emitting energy sources. Over the last decade, the deployment of electrochemical energy storage devices in the transport and energy sector has increased significantly. Numerous devices can be used for low-emission energy storage and power delivery with the optimal technology dependent on the requirements of the application. These devices include hydrogen fuel cells, redox flow batteries and supercapacitors, as well as the ubiquitous lithium-ion battery (LIB). LIBs have been deployed in a diverse range of applications, from personal electronics to electric vehicles and stationary storage applications to mitigate intermittency in renewable energy generation.

Despite the success and continued improvement in LIBs, there remain some challenges. The main issues with current generation LIBs are related to safety, specific energy as well as the toxicity and resource scarcity of some of the components, particularly in relation to the nickel and cobalt contained in many LIB chemistries. The specific energy of Li-ion cells is limited by the use of a graphite negative electrode which offers a theoretical capacity of 372 mAh g^{-1}. As such, alternative battery chemistries that can combat some of these issues, and in particular the specific energy, must be targeted for the continued electrification of the most challenging applications, such as heavier vehicles and aerospace.

The range of these "next-generation" chemistries that are currently under investigation are extensive. They include, but are not limited to, zinc-ion and -air, lithium-air, sodium-ion and cells which utilise lithium metal negative electrodes, each with their own potential advantages and disadvantages. Of these next-generation chemistries, one of the most promising candidates is the lithium sulfur (Li-S) battery. Lithium-sulfur batteries generally consist of a carbon/sulfur positive electrode and a lithium metal negative electrode with an ether-based electrolyte.[1] The combination of these materials, which excludes any transition metals in the active components, has the potential to have a significant impact on both the issues associated with resource scarcity and the environmental impact of both battery production and recycling.[2] The nature of the lithium-sulfur chemistry means that these cells also lend themselves to applications requiring low specific energy densities with realistic specific energy densities in the region of 600 Wh kg^{-1}, likely practically achievable for cells with a liquid electrolyte.[3]

Despite the promise of lithium-sulfur, and the significant advances towards a commercialisation made in recent years, there are still some issues that must be overcome if the technology is to be commercialised. These issues consist of a currently limited cycle life relative to lithium-ion cells, with the main causes of this short life span attributed to the polysulfide shuttle reaction and the formation of lithium dendrites which results in electrochemically "dead" lithium.[4] Due to the nature of the chemical reactions occurring during the charge and discharge there are also limits on the power output of the cell, or attenable "C-rate." In order to drive this chemistry towards a commercially viable and relevant product, these issues must be addressed and overcome. A key strategy to combating these issues is an improved understanding of how these processes occur while the cell is operating.

Numerous studies have focused on the use of ex situ measurements to gain a greater understanding of the operation of lithium-sulfur cells. While ex situ studies can provide highly insightful information about the operation of cells, they often require the destructive disassembly of the cell and are limited by the time taken to prepare samples for study and the potential impacts this might have on the characteristics of the materials compared to when you are under operating conditions. As a result of these limitations, some of the results obtained may be misleading.

Analysis of a cell in situ/*operando* provides more insightful information about the processes occurring and allows, more easily, for the correlation of the analytical data obtained with electrochemical data that can be collected concurrently. While the development of in situ cells (cells specifically designed for measurements of

[z]E-mail: rhodri.owen@ucl.ac.uk; j.b.robinson@ucl.ac.uk

this nature) has developed at pace, there are still some potential issues with ensuring that the design of the cell provides an environment for the materials that is as close as possible to a realistic cell.

In recent years there has been significant focus on the use of in situ techniques for understanding processes occurring during lithium-sulfur cell operation. One of the main areas of focus for in situ studies has been the use of Raman spectroscopy, where the combination of chemical species information and the in situ nature of the measurements has led to a deeper understanding of the mechanisms at play in lithium-sulfur systems.[5] Other techniques conducted in situ include, but are not limited to, X-ray diffraction (XRD),[6] X-ray absorption spectroscopy (XAS),[7] transmission electron microscopy (TEM),[8] atomic force microscopy (AFM),[9] X-ray radiography,[10] X-ray computed tomography (XCT),[11,12] UV-Vis,[13] FTIR.[14] A recent review on in situ measurements conducted by Rehman and co-workers concluded that while there are some compromises on battery chemistry required for in situ measurements, the insights derived make them essential for further development of the lithium-sulfur battery. However, to meet the widespread use requirements, low-cost techniques should be prioritised.[15]

One low-cost, easily accessible, *operando* technique that is gaining growing interest is the use of *operando* optical microscopy to observe and understand the processes occurring in cells during charge and discharge. Numerous studies have monitored the lithiation and delithiation of lithium-ion graphite anodes based on the colour change of the graphite. Recent studies on this concept have shown that it can provide interesting information related to fast charging regimes and when combined with modelling can be a powerful tool for predicting cell behaviour.[16] The increasing number of *operando* optical microscopy studies is not limited to LIB chemistry with several papers focusing on the formation of lithium dendrites in lithium metal batteries[17] and studies into the formation of dendrites in zinc-based systems.[18,19]

Lithium-sulfur batteries have received limited attention in the field of *operando* optical microscopy. Some attention has been applied to all-solid-state lithium-sulfur batteries, where the technique allowed direct tracking of the structural evolution at the solid-solid interfaces and the identification of irreversible transformation linked to the volume expansion of the lithium metal and phenomena related to the polysulfide shuttle.[20] A few studies have also relied on the change in colour of the electrolyte based on the formation and the change in length of the polysulfide intermediates to track and monitor the reaction.[21,22] To the authors' knowledge, the liquid electrolyte-based lithium-sulfur system has not been studied as a whole. Studying all components of the cell concurrently will allow for the correlation between behaviours observed at the anode, cathode, in the electrolyte as well as with the electrochemical data.

This paper focuses on the *operando* optical microscopy of full lithium-sulfur cells during operation at various current densities, in order to visualise the effects of C-rate. Following on from work published recently,[16,19] the observations are quantified so that different datasets can be effectively compared quantitatively rather than just qualitatively.

Materials and Methods

Operando measurements were conducted using an ECC-Opto-Std test cell designed for optical and X-ray characterization (EL-CELL, Germany). The cell was set-up in side-by-side mode with 14 mm half circles of electrodes. Figure 1 shows the set-up of the *operando* cell with an exploded view in Fig. 1a showing the main components of the cell, illustrating how the electrodes and separator were orientated. An assembled view and top-down view of the cell are shown in Figs. 1b and 1(c) with (c) illustrating how the two electrodes and separator are visible when fully assembled.

The cathode used for this study was NANOMYTE BE-70E, a sublimed sulfur tape obtained from NEI Corporation, US. The electrode consisted of a 16 μm carbon-coated aluminium current collector with a coating containing 65% active material 10% CMC-SBR binder and 25% carbon black, a sulfur loading of 3.75 mg cm^{-2} ± 5% is reported by the manufacturer. The anode was cut from lithium foil, 120 μm thick (Goodfellow Advanced Materials, UK). A 1 mm thick, 10 mm diameter glass fibre disc was as used as a separator (EL-CELL, Germany). The electrolyte consisted of 1 M bis(trifluoromethane)sulfonimide (LiTFSI, dried, Sigma Aldrich) and 0.8 M lithium nitrate ($LiNO_3$, dried, Sigma Aldrich) dissolved in a 1:1 volume ratio of 1,3-dioxolane (DOL, anhydrous, Sigma Aldrich) and 1,2-dimethoxyethane (DME, anhydrous, Sigma Aldrich). All solvents were dried over 4 Å molecular sieves for over three days before use. All materials were handled, and the cell was assembled in a glovebox under an argon atmosphere where water and oxygen levels were maintained at below 0.5 ppm. The cell was assembled as shown in Fig 1, first the glass fiber separator was placed on the base of the cell with the two electrodes placed on top with a small gap between them. A sapphire window was placed on top of the electrodes and separator. A seal between the sapphire window and the cell body was achieved with an O-ring with the window and O-ring held in place with a metal cell cover (Fig. 1a-2). Once the cell was sealed two contact pins (Figs. 1a-9 and 11) were screwed in place to establish an electrical connection to each electrode. Finally, electrolyte sufficient to flood the cell was used to remove all gases and obtain clear images was added and the cell was sealed using a stopper (Fig. 1a-10). It should be noted that flooding the cell in this manner requires ca. 100 μL of electrolyte and does result in a high E/S ratio (ca. 8.7 μL/mg$_s$) which is unrealistic for commercial cells; however, this was necessary in order to obtain clear images. With the cell fully assembled and sealed, it was safe to remove from the glove box for testing and optical imaging.

Optical imaging was conducted using a 4 K Keyence VHX-7000 digital microscope. A X150 objective lens was used to obtain a field-of-view (FOV) of ca. 2 by 1.5 mm. Images were recorded every 60 s. Electrochemical testing was conducted using an Interface 1010 potentiostat (Gamry, USA). Cells were cycled between 1.8 and 2.8 V at various currents. Currents were calculated based on current density obtained by using the working face of the lithium electrode (14 mm wide × 120 μm thick).

Raman spectroscopy mapping was conducted using a Thermo Scientific DXR Raman spectrometer with a wavelength of 532 nm at Raman shifts between 100 and 3500 cm^{-1}. Raman spectra were taken in a grid pattern with an x and y spacing of 10 μm. The cathode samples were removed from the cell, washed with a DOL:DME (1:1 by volume) solution to remove soluble components and electrolyte salts before drying and subsequent analysis using Raman spectroscopy.

The datasets were batch-processed using custom Python code which segmented them using the Otsu method.[23] To account for varying quantities of the lithium foil being observed the optical image was cropped so that 300 pixels either side of the boundary between the lithium and the separator made the whole image. The image was then segmented to areas that consisted of lithium and those that contained no lithium, this quantity was set as a lithium fraction of 0.5, values below this value indicate lower quantities of lithium and values above 0.5 indicate larger quantities of lithium. This normalised value of 0.5 indicates that half of the cropped image used for analysis is lithium initially and is a relative value that can be used to compare across samples. Normalised grey intensity values were calculated using custom Python code which converted the obtained image to grey scale and used an average of 50 pixels to obtain the grey scale value.

Results and Discussion

To gain a deeper understanding of the processes occurring within a lithium-sulfur cell, *operando* optical microscopy was conducted as outlined in the materials and methods section. Initially, an areal current density of 1 mA cm^{-1} was chosen. Due to the nature of the side-by-side set-up of the optical cell the current density was

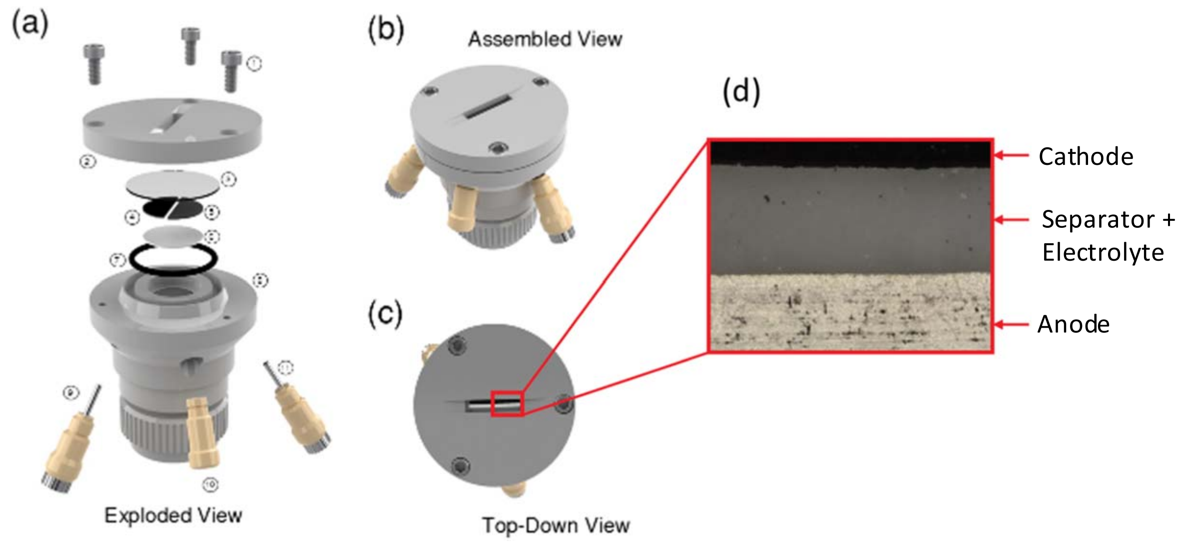

Figure 1. (a) Exploded view of cell used for *operando* optical imaging of the lithium-sulfur cell in side-by-side mode. The cell consists of ① bolts to hold the top and bottom of the cell casing together ② the top of the cell casing ③ transparent glass window to allow viewing of electrode without exposure to air ④ half circle of S-C cathode material ⑤ half circle of lithium metal ⑥ disc of separator ⑦ O-ring for formation of a seal between the bottom cell casing and glass viewing window ⑧ the bottom section of the cell casing ⑨ cathode contact pin ⑩ plug to seal electrolyte filling port ⑪ anode contact pin. (b) a view of the assembled cell and (c) a top-down view of the cell as seen by the microscope with both electrodes and separator visible through the viewing port and glass slide. (d) The view of the electrode obtained while imaging with the component parts labelled.

calculated based on the area of the lithium negative electrode that was in contact with the electrolyte, i.e. the thickness of the foil multiplied by the diameter of the half lithium disc used for the anode (see Fig. 1 for reference).

As assembled, the cell was fully charged at the start of the testing with a voltage of approximately 3.1 V, as seen in Fig. 2a. The evolution of the cells condition can be observed by following the time steps shown in Fig. 2. Here, the black strip across the top of the image is the sulfur-carbon positive electrode and the metallic strip at the bottom is the Li negative electrode. The region between the two electrodes, with a distance of ca. 400 μm shows the electrolyte-soaked glass fibre separator. Initially, the electrolyte is colourless as it only contains the $LiNO_3$ and LiTFSI salts dissolved in the DOL:DME solvent mixture. If the cell is left in this assembled state no changes in appearance are observed, even after extended periods of time (24–48 h). This demonstrates that the changes observed as the cell is cycling is related to the electrochemical changes occurring and is reflective of the slow dissolution dynamics of $S_{8(s)}$ into the DOL:DME electrolyte.

Figure 2a shows optical images of how the cell changes over the initial 18 min of discharge. Almost immediately after discharge begins the electrolyte close to the cathode begins to show a change in colour with a yellow wave extending from the sulfur-carbon electrode. After 4 min there is a clear region extending ca. 100 μm from the positive electrode which has become yellow in colour. This change in electrolyte from colourless to yellow can be attributed to the solubilisation of the sulfur contained within the cathode as it is converted from $S_{8(s)}$ into Li_2S_8 and shorter polysulfides which possess a higher solubility in the chosen electrolyte solvents compared to elemental sulfur. This front of coloured electrolyte moves across the separator and towards the lithium anode as the discharge proceeds and more of the $S_{8(s)}$ contained in the cathode is converted into polysulfide species. By ca. 12 min into the initial discharge all the electrolyte appears yellow in colour. At this point there is still a colour gradient between the two electrodes; however, after a total discharge of 16–18 min the colour across the interelectrode distance appears almost uniform.

Figure 2b shows a plot of how the cell voltage varies over the first discharge. As is commonly observed in lithium-sulfur systems, the voltage initially drops rapidly from ca. 3.1 V to 2.35 V, at this point the rate of voltage drop decreases significantly. When comparing Figs. 2a and 2b it is evident that the initial colourisation of the electrolyte happens rapidly and is completed within the first 2% of discharge time and corresponds to the initial rapid drop in voltage.

As observed in Fig. 2d, although the full interelectrode space becomes yellow in colour within the first ca. 18 min of discharge as sulfur is converted into long-chain polysulfides, this yellow colour does not stay constant throughout the rest of the discharge. This change in colour can be attributed to two primary factors, (i) the concentration of polysulfides in the electrolyte, this can be attributed mainly to the change observed over the initial 65 min, and (ii) a change in the chain length of the polysulfide species. As a lithium-sulfur system is discharged the elemental sulfur is initially converted to Li_2S_8, as the discharge progresses this long-chain polysulfide is further reduced to progressively shorter polysulfide species ($Li_2S_8 \rightarrow Li_2S_6 \rightarrow Li_2S_4 \rightarrow Li_2S_2$). This change in length of the polysulfides results in a change in the bulk colour of the electrolyte since shorter-chain polysulfides appear lighter in colour than their longer chained variants.[21]

This change in electrolyte colour can be quantified through the use of a normalised grey intensity (NGI) using methods similar to those demonstrated in the work of Blanchard et al.[21] and Sun et al.[22] To calculate the normalised grey intensity the optical image is first converted from a colour image to greyscale, following this the greyscale values were normalised to their initial value. A number of pixel values were taken and averaged to calculate the values across the interelectrode gap, with the variation in values in positions both near the positive electrode (blue line) and the negative electrode (red line) shown across the discharge in Fig. 2c with the initial lightest value giving a value of 1 and lower values indicating darker electrolyte solutions.

As shown in Fig. 2c, as discharge begins there is an initial decrease in the NGI in Region 1. This decrease in NGI indicates that the colour of the electrolyte is getting darker, this can mainly be attributed to the initial transition from a colourless electrolyte to the yellow, polysulfide-containing solution. The fact that the electrolyte appears to be a mainly uniform colour in the optical images shown in Fig. 2a after 18 min but the NGI continues to decrease until ca. 65 min indicates that this cannot be the only contributing factor. This continued decrease in Region 1 is likely attributable to an increasing concentration in polysulfide species. The region closer to the cathode, where the sulfur species originate reaches the minimum

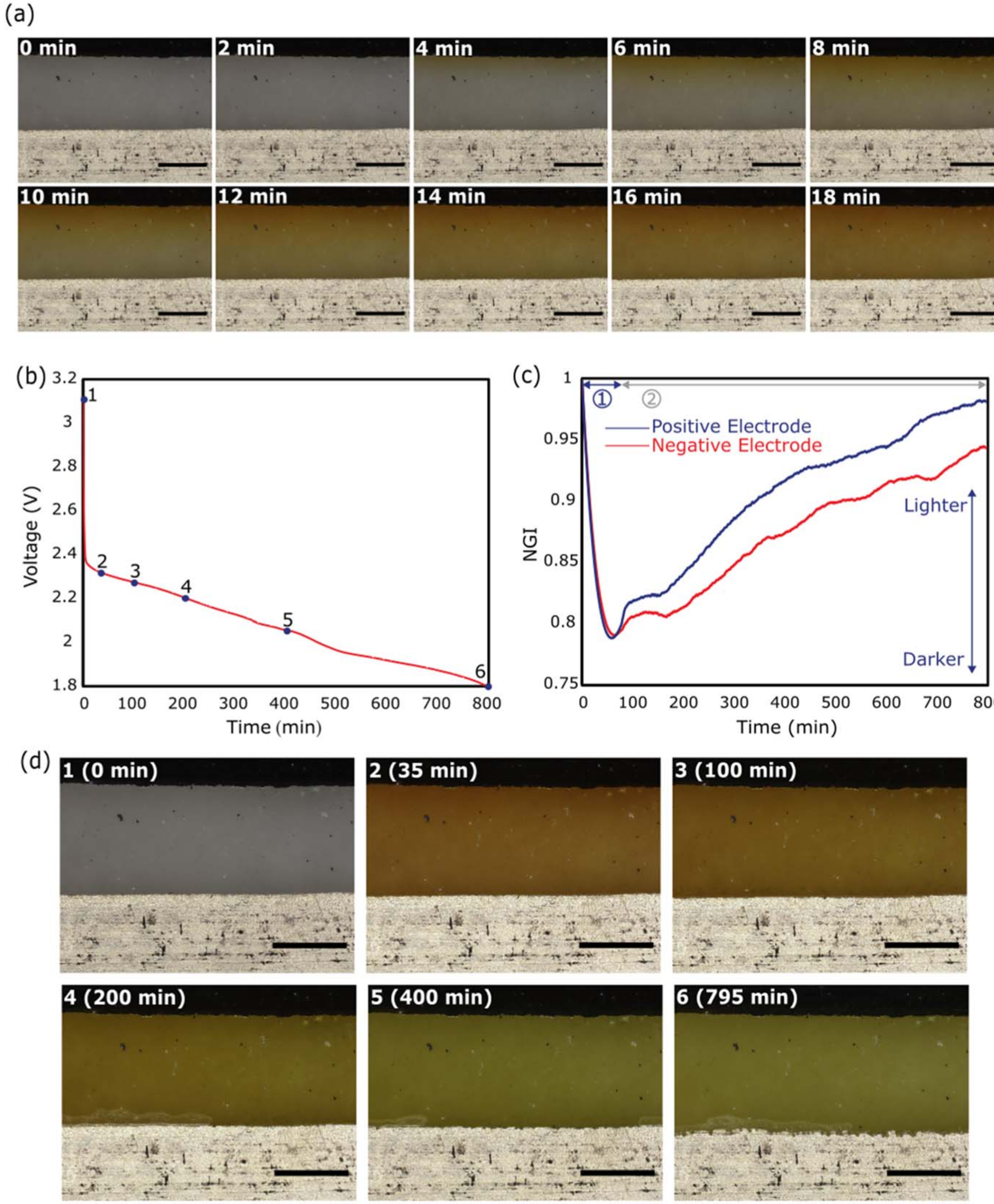

Figure 2. (a) Optical images recorded during the first 18 min of discharge, showing the colour change of the electrolyte. (b) Voltage profile of *operando* cell's first discharge. (c) The variation of normalised grey intensity values across the first discharge. (d) Optical images at various points across the first discharge, the time at which each numbered image was recorded is shown in (b) of this figure. Scale bar = 500 μm.

NGI value before the position closer to the negative electrode, as would be expected due to mass transport limitations.

After both positions have reached a minimum NGI value both begin to increase as highlighted as Region 2 in Fig. 2c. This decrease in NGI is as would be expected for a system where the darker longer chained polysulfides are being converted into the lighter shorter chain polysulfides and subsequently precipitating out of solution. It is likely that this conversion of longer to shorter chain polysulfides may have been preceding before Region 2; however, the effect was masked by the concentration changes occurring in the electrolyte.

In order to quantify the amount of lithium present in the system, the region closest to the lithium negative electrode was isolated for each image, with an equal amount of the image representing both the electrode and the interelectrode space selected. This resulting image was then binarised, using the Otsu method,[23] into regions which contained lithium and those which did not, enabling the calculation of normalised lithium fraction for this selected region. As a result of this approach the initial value was 0.5 Li for the fresh cell. Figure 3 summarises the data obtained in this analysis step with example segmented images obtained at four time steps shown in (c) and the variation of the normalised lithium fraction across the course of the first discharge shown in Fig. 3b. Initially a slight increase in the lithium fraction can be seen. While it is not clear what process contributes to this, it is likely that the initial change in colour of the electrolyte solution as the reaction proceeds has a minor impact on the segmentation (see SI Fig. 1). Despite this unusual behaviour it is clear the magnitude of the effect is small compared to the change observed in the lithium fraction over the course of the full discharge. As the voltage reduces from ca. 2.4 to 1.8 V the lithium fraction can be seen to decrease as would be expected. This voltage change is expected to predominantly correspond to the conversion of elemental sulfur to long-chained polysulfides and the reduction of larger polysulfide molecules to shorter-chained variants. This expectation is in keeping with the colour change observed in the electrolyte in Fig. 2. This conversion of longer-chained polysulfides to shorter-chained polysulfide requires the consumption of lithium from the negative electrode since two lithium ions are required for each longer-chained polysulfide to be split into two shorter chains. As shown in Figs. 3b and 3c this consumption of lithium from the anode results in stripping of the metallic lithium for the anode, resulting in a contraction of the electrode [shown in yellow in figure (c)]. This contraction of the electrode is quantified in Fig. 3b which shows a relatively linear drop in normalised lithium fraction from 0.5 to *ca.* 0.38 at the end of discharge (as set by the 1.8 V cut-off voltage).

It should be noted that the voltage discharge curve (Fig. 3a), deviates slightly from what is typically reported for lithium sulfur systems where a more distinct two plateau appearance is typically observed.[1] This difference can likely be explained by the relatively large excess of sulfur in the cathode due to the fact that current density is calculated based on the active area of the negative electrode. While not all of the sulfur is accessible due to only part of the electrode being exposed to the required conditions, it may have some influence on the cell's voltage profile.

After the cell was discharged to 1.8 V, as per the cycling protocol, the cell was then charged at the same current density ($1\ mA\ cm^{-2}$). As the cell is charged the voltage increases as would be expected with the voltage profile shown in Fig. 4a. Initially the voltage increases rapidly as is commonly reported in the literature for lithium-sulfur systems. It should be noted that cell specific overpotentials are likely to manifest in this region which may offset the expected voltage of processes. After this initial increase it gradually increases further with two apparent plateaus observed in the voltage curve at ca. 2.3 V and ca. 2.4 V respectively.

As the charge of the lithium-sulfur system progresses, the Li_2S and short chain polysulfides present at the end of the first discharge begin to be re-oxidised into longer chained polysulfides en route to the final S_8 product which would be expected in a fully charged system which retained high Coulombic efficiency. In keeping with the observations reported for the cell's discharge, this change in chain length and concentration of lithium polysulfides is expected to result in a change in the colour of the electrolyte in the interelectrode space. NGI values for positions close to the positive electrode (blue line) and close to the negative electrode (red line) have been calculated and are plotted in Fig. 4b.

For both positions, the calculated NGI values decrease as the cell charges. This decrease in NGI indicates that the electrolyte is getting darker in colour; this corresponds to the processes expected as the

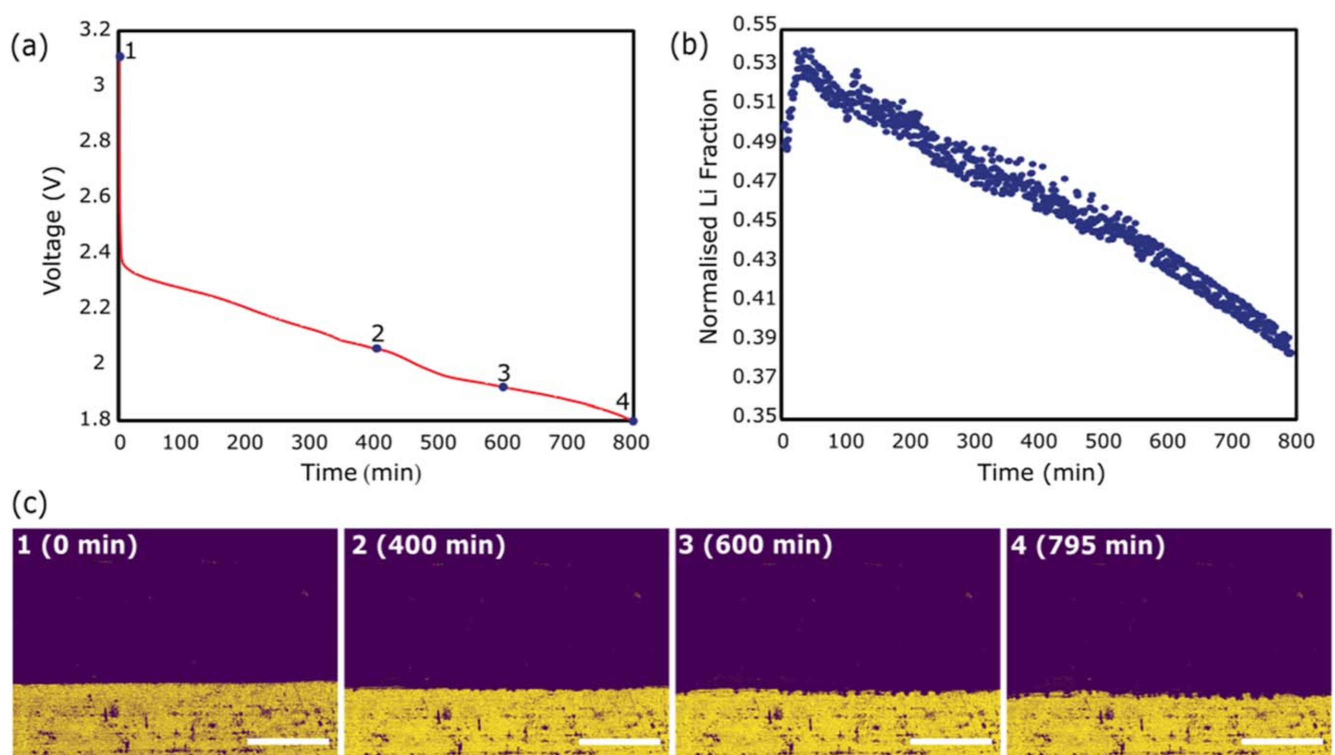

Figure 3. (a) The cell's discharge voltage profile with four points in the discharge curve highlighted. These highlighted periods of the discharge correspond to the segmented images shown in (b). (b)The yellow regions in these segmented images represent the lithium fraction, whereas the blue regions represent the rest of the cell components. (c) A plot showing the variation of the normalised lithium fraction and its variation across the duration of the first discharge. Scale bar = 500 μm.

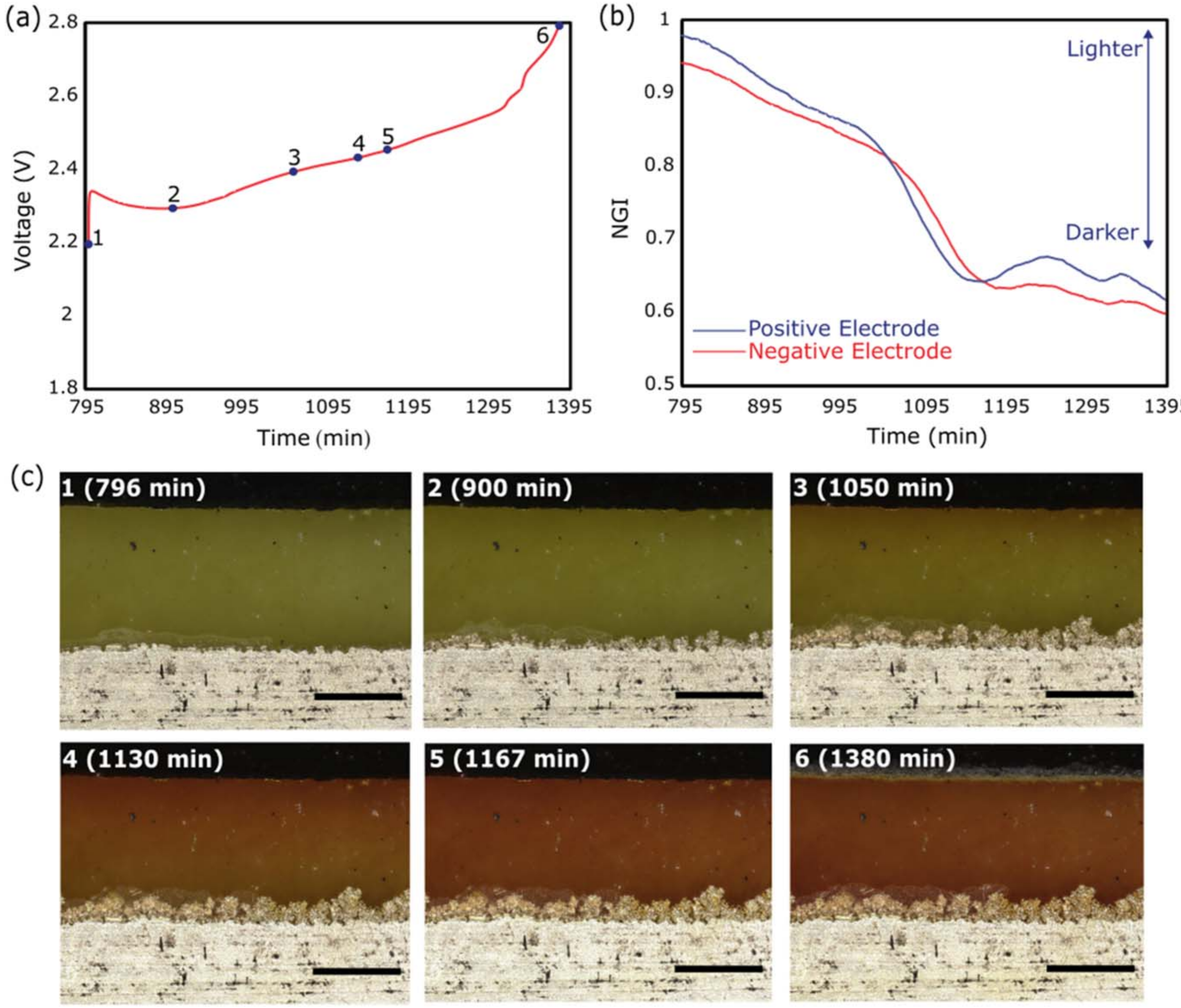

Figure 4. (a) the voltage profile of the lithium-sulfur cell's first charge at a current density of 1 mA cm^{-2} with selected points where the optical images showing in (c), highlighted. (b) The normalised grey intensity (NGI) values calculated for two positions in the interelectrode space. (c) optical images obtained at various points across the first charge of the lithium-sulfur cell highlighting the colour changes and morphological changes occurring in the system. Scale bar = 500 μm.

lithium polysulfide chain length increases. The position closest to the positive electrode (blue line – Fig. 4b) starts with a lighter colour (i.e. higher NGI) than the position closest to the negative electrode and reaches a minimum NGI value faster than the negative electrode position. Although slightly delayed relative to the positive electrode, the negative electrode position shows a similar trend. This spatial variation highlights the impact of diffusional limitations through the interelectrode space particularly under these conditions where the cell switches from discharge to charge without a rest period. As noted previously the format of the cell used in this work necessitates large electrolyte volumes so the magnitude of these differences is likely exaggerated when compared to an optimised cell geometry.

Interestingly, for both systems the minimum NGI value is reached after 300–350 min, corresponding to a voltage of ca. 2.4 V, approximately mid-way through the second voltage plateau. After this minimum is reached the NGI for positions close to each of the electrodes remains relatively constant, with no colour change indicating no significant changes in the length of the polysulfide chains or the net concentration of the species present in the electrolyte. The retention of colour in the electrolyte following the discharge/charge cycle highlights the inability of the cell to reconvert all of the polysulfides to elemental sulfur. While this does not directly correlate with a loss of active material, the presence of lithium polysulfides in the electrolyte increases the likelihood of polysulfide shuttle and loss of active material at the Li negative electrode. Indeed, the extent of the colour change could be used as a proxy for the first cycle efficiency which has been shown to have a significant impact on the overall lifetime of cells.[24]

Figure 4c shows images recorded at several points across the course of the first charge of this system. The points at which each of these images were recorded and the corresponding cell voltage at this point are indicated in the voltage profile curve shown in Fig. 4a. From these images the colour change quantified in Fig. 4c can be observed. Little to no obvious change in the colour of the interelectrode space is observed after image 4 (corresponding to the plateau observed in Fig. 4b) supporting the results quantified in this plot.

As the cell is charged and the polysulfides are oxidised toward longer-chained molecules, lithium ions are evolved and plated onto the surface of the negative electrode as metallic lithium. At 1 mA cm^{-2}, this results in the formation of "tree-like" dendritic lithium structures on the surface of the electrode, as observed in Fig. 4c. The formation of these dendrites occurs relatively quickly after the charge of the lithium sulfur system is initiated with their growth continuing throughout the charge, until the features stabilise, as can be seen in Images 4–6 of Fig. 4c.

In order to quantify the deposition of lithium onto the anode, the lithium fraction of the sample was again calculated through segmentation, with the results from analysis shown in Fig. 5. The high surface area of the dendrite and their heterogeneous morphology reduces the accuracy of the segmented data due to the limited pixel resolution of the image and segmentation method; further work is ongoing to continue to optimise the resolution which can be obtained using this method.

The normalised lithium fraction over the course of the charge is shown in Fig. 5b, with snapshots of the segmentation shown in Fig. 5c, 1–4. The timing of these snapshots is highlighted on the charge curve shown in Fig. 5a. As soon as the charge begins, the normalised lithium fraction increases in a linear fashion with a maximum value of ca. 0.55 observed, slightly higher than the initial value of 0.5 which is obtained using this approach in the fresh cell. A similar trend to that observed in Fig. 4b can be seen after approximately 300–350 min of charging when the normalised lithium fraction plateaus. This suggests a stabilisation in the features over this time period.

By quantifying the changes in electrolyte colour and the lithium fraction rather than assessing them with qualitative observation we are able to highlight a change in the condition of the cell that is not readily evident in the electrochemistry, i.e. the evolution and stabilisation of lithium filaments at the negative electrode. The lack of further significant changes in the normalised grey intensity and normalised lithium fraction indicates that the processes the cell is undergoing at the end of the charge cycle are no longer proceeding to the same extent or at the same rate. This suggests that the termination of charge is not caused by processes that occur within the electrolyte or in the interelectrode space for this system. Further, the termination of charge evidently occurs before all of the polysulfides have been reoxidised to elemental sulfur suggesting that the positive electrode is the charge limiting electrode. This suggests that either a loss of accessible electrical conductivity or electrode porosity likely results in the increase in polarisation which causes the voltage rise in Fig. 5a. To explore this further, investigations were undertaken to determine any other changes that may be occurring within the cell during this period. Throughout the course of the initial discharge and the initial charge period there is little to no change observed in the appearance of the positive electrode or the positive electrode/electrolyte soaked separator interface. However, at the top of charge this no longer holds true with the appearance of solid yellow deposits at this interface. For clarity, a magnified region of this interface across the final 200 min of the charge, approximately equivalent to the plateaus observed for the NGI and normalised lithium fraction, are shown in Fig. 6a. As shown, initially at 1180 min, the positive electrode appears as it has for the rest of the experiment. However, the deposition of this yellow solid across this period can be clearly observed in these magnified images (Fig. 6a).

In order to identify the composition of these yellow deposits and the composition of the fresh positive electrode, samples of both the fresh electrode and one taken from the cell after cycling were analysed using Raman spectroscopy. Mapping of selected peaks was conducted to understand the spatial distribution of components on the surface of the electrode. Raman spectroscopy of the fresh positive electrode sample varied depending on the location but mainly consisted of peaks attributable to both carbon and sulfur present in its S_8 form. A typical spectrum for a sulfur rich region of the fresh cathode is shown in Fig. 6d. Here, peaks present at ca. 150 cm^{-1}, 220 cm^{-1} and 474 cm^{-1} can be attributed to S_8.[6,25] Even in the sulfur-rich regions peaks at ca. 1200 and 1600 cm^{-1}, attributable to carbon, are still observed.[26] To generate maps representative of the sulfur and carbon positions, the intensity of peaks at 220 cm^{-1} (S_8) and 1200 cm^{-1} (C) were chosen (peaks highlighted in Fig. 6a). The resulting maps from the fresh positive electrode are shown in Fig. 6b.

In the fresh positive electrode sample, Fig. 6b, a broad distribution of both sulfur and carbon is observed across the electrode surface with only the top left region, which does not contain the

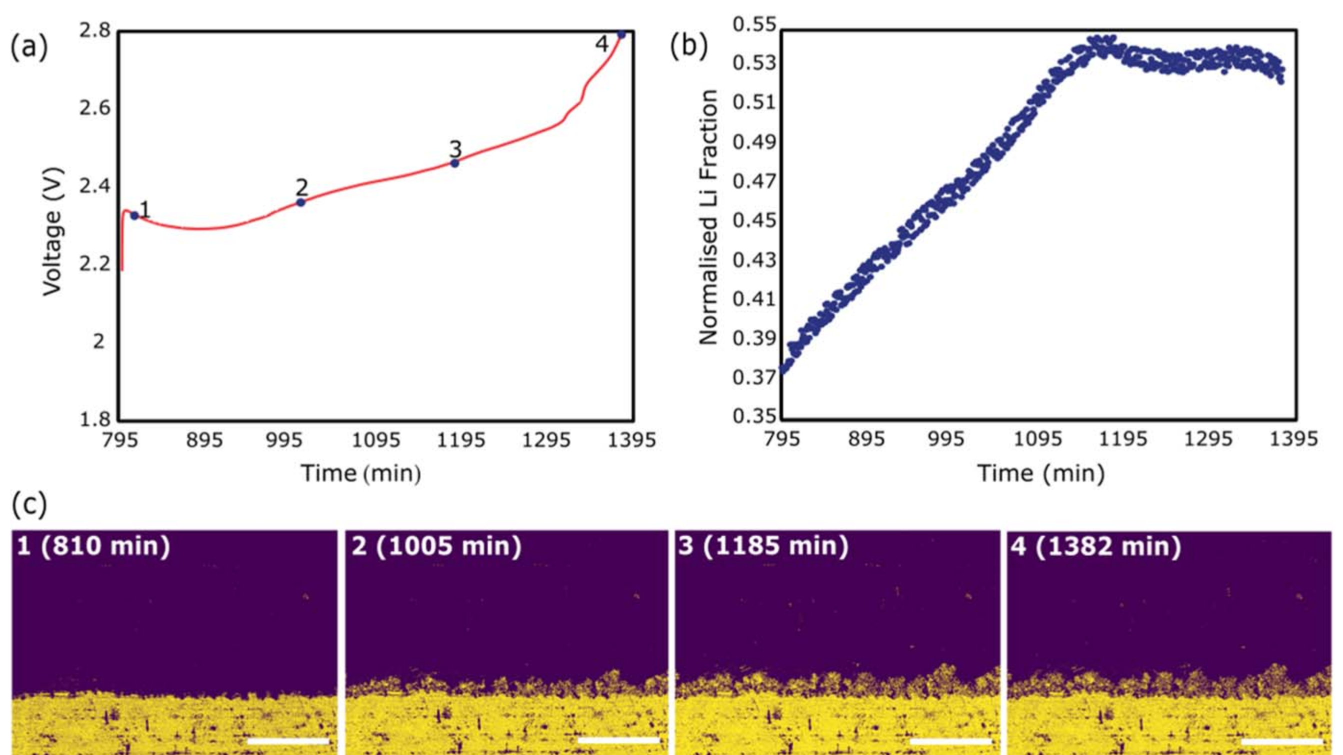

Figure 5. (a) The voltage profile for the first charge of the lithium-sulfur cell with the points at which example segmentation images (shown in (c)) highlighted. (b) The variation of the normalised lithium fraction across the course of the first charge (c) Example images of the results of the segmentation process used to calculate the normalised lithium fraction. Scale bar = 500 μm.

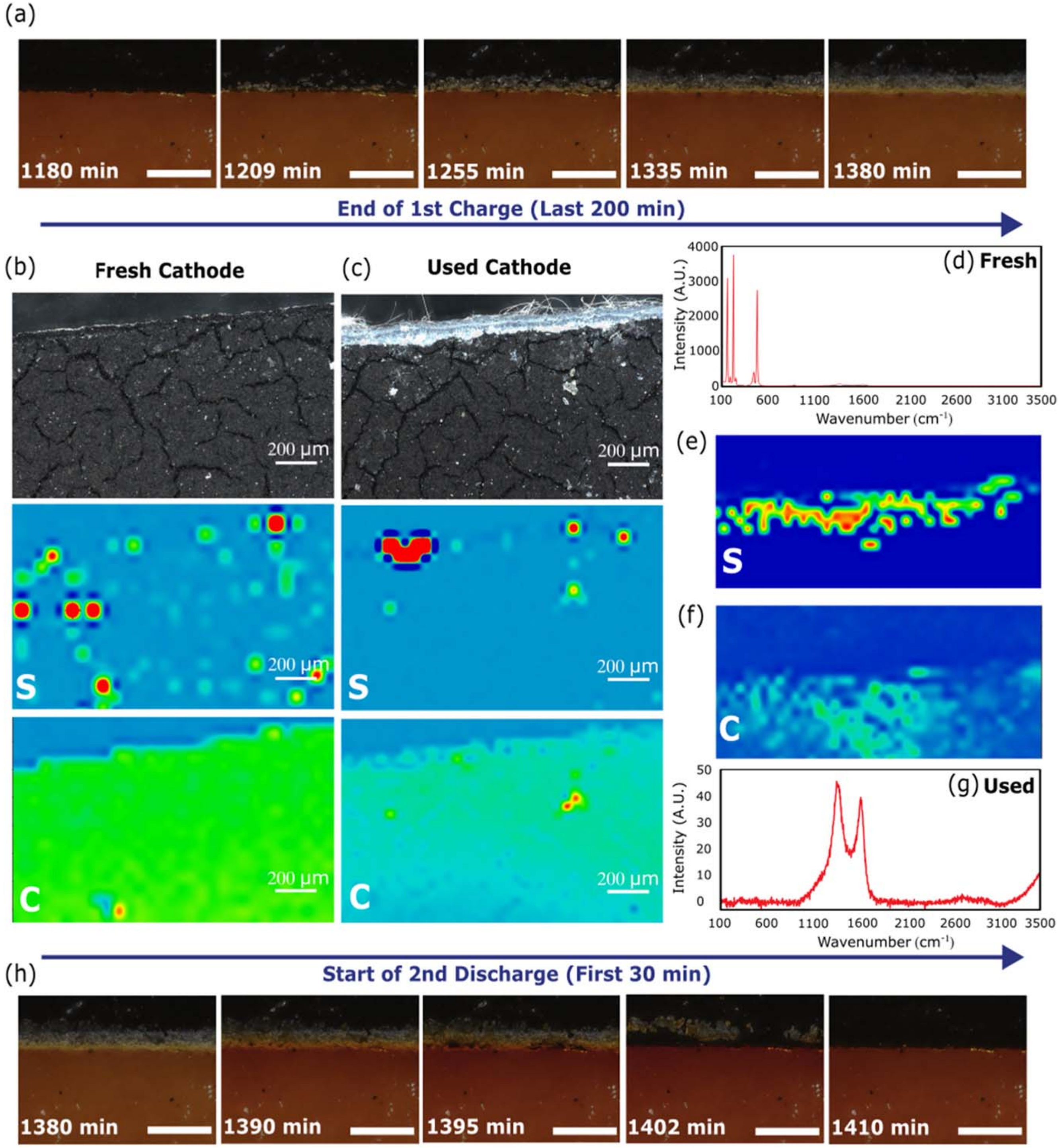

Figure 6. (a) Increased magnification images showing the development of deposits on the cathode electrolyte interface over the course of the final 200 min of the first charge. Optical images and Raman spectroscopy mapping of the sulfur and carbon positions for the fresh cathode (b) and the cathode after five cycles at 1 mA cm^{-2}. Typical Raman spectra for both the fresh and used samples, with the peaks mapped highlighted are shown in (d) and (g) respectively. (e) and (f) show lower magnification mapping of the carbon and sulfur locations on a used electrode, demonstrating that the results in (b) and (c) are not isolated to one region of the electrode. (h) higher magnification images of the cathode/electrolyte interface showing the dissolution of the deposits over the course of the first 30 min of the following discharge. Scale bar = 500 μm, unless stated otherwise.

electrode, showing the absence of these peaks. In contrast, the maps produced from the used electrode sample (after 5 cycles at 1 mA cm^{-2}) vary significantly. The carbon distribution remains constant with no significant variation from the fresh sample. A typical Raman spectrum from this mapping study is shown in Fig. 6g. Here, as for most of the electrode surface, only carbon is detectable, suggesting that the majority of the S_8 visible in the initial fresh sample has been consumed and converted into polysulfide over the course of the first five cycles, even at distances relatively high (~800 μm) from the electrode front where the majority of the chemistry would be expected to occur.

At the top of charge (the SoC this electrode was at) significant quantities of S_8 sulfur would be expected in the positive. Figure 6c shows the spatial distribution of the same S_8 species detected in the

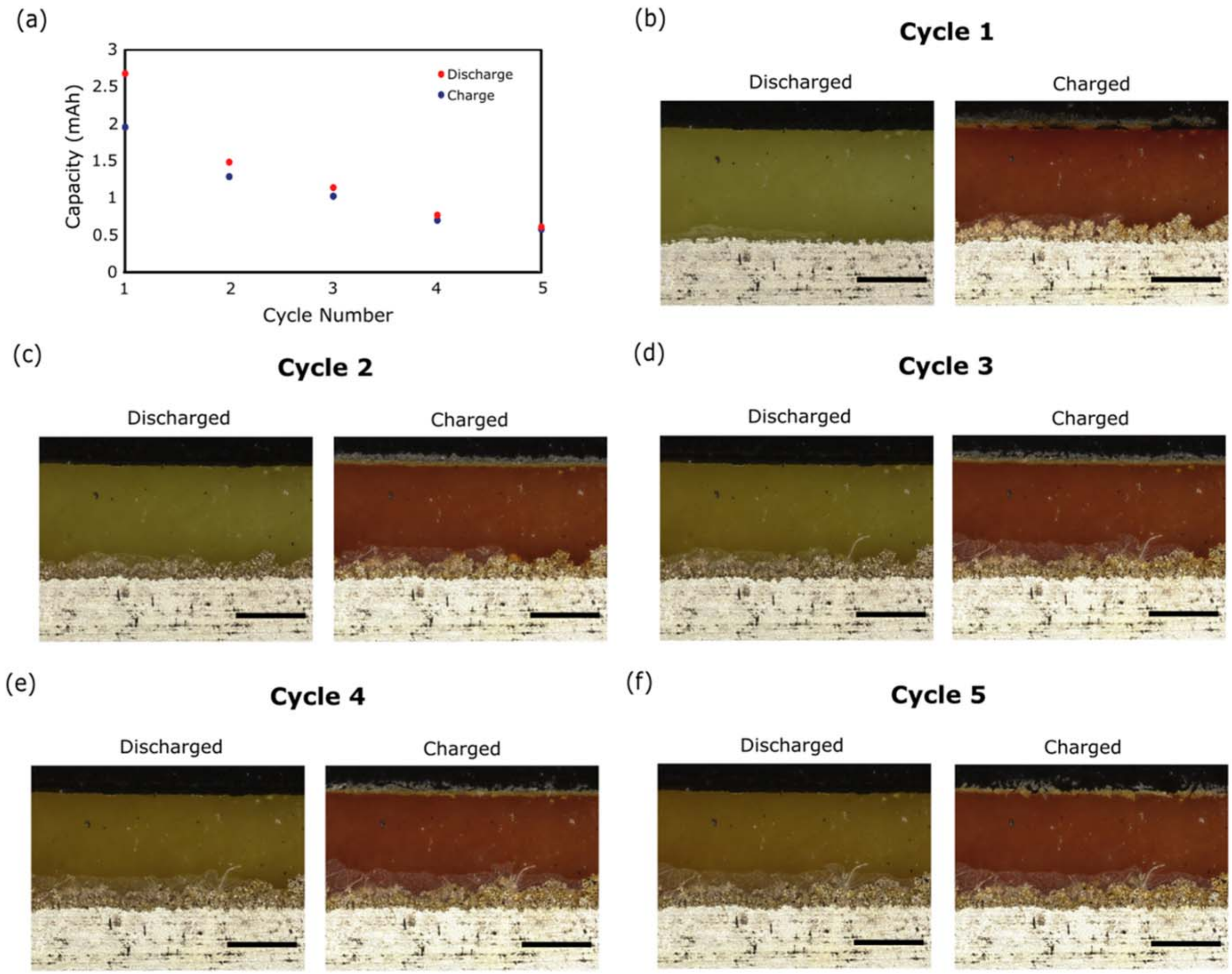

Figure 7. (a) Cell capacity as a function of charge and discharge cycle when operated at 1 $mAcm^{-2}$. (b)-(f) Optical images showing the appearance of the bottom of discharge and top of charge for the first five cycles of the lithium-sulfur test cell. Scale bar = 500 μm.

fresh sample. From these plots, we can determine that the vast majority of the S_8 sulfur has been deposited at the edge of the electrode. This suggests that at the top of charge, the rate of charge is sufficient to limit the majority of the conversion from long-chained polysulfide is occurring at the electrode/separator interface. This S_8 deposition and conversion from soluble polysulfides into insoluble precipitants accounts for the yellow deposition observed in the optical microscopy. This is further supported by lower magnification mapping (Figs. 6e and 6f) which clearly shows the sulfur front across the electrode, separator interface.

The data summarised in Fig. 6 suggests that the deposition is related to the precipitation of solid S_8 sulfur. This represents the final chemical process in the simplified charge regime of the lithium-sulfur battery. As noted earlier, the onset of this deposition corresponds to the plateaus observed for both the NGI and the normalised lithium fraction. This suggests that when the cell reaches this point in the charge curve the majority of the shorter chained polysulfides have been converted to the longer Li_2S_8 and this final stage of the charge process is dominated by the transition from solution-based reactions to the precipitation of solid S_8 which accounts for the limited change in the NGI, normalised lithium fraction and the observed deposition steps. It is also possible that the deposition of sulfur in this manner may be passivating the electronic surface of the positive electrode, in turn limiting the extent of the solution-based reactions that are being monitored using the NGI.

When the cell is subsequently discharged for a second time after the completion of the first charge step this yellow deposition is rapidly consumed, as shown in Fig. 6h. The dissolution of the S_8 occurs over a period of approximately 30 min, compared to the 3,000 min taken for its formation during charge. This dissolution is expected if, as suggested, the deposition is S_8, since the first step of discharge is the conversion of the solid S_8 into soluble polysulfide species.

To quantify the changes occurring as the cell is cycled, the NGI and normalised lithium fraction was calculated, as shown in Fig. 8, along with the cells' voltage profile across this test. The NGI is shown in Fig. 8b for two locations, one close to the positive electrode (red) and one close to the negative electrode (blue). As expected, an oscillating pattern is observed that correlates to the voltage profile showing that in general as the cell is discharged the NGI increases, the electrolyte gets lighter and that as the cell is charged the NGI decreases indicating darker electrolyte with longer chained polysulfides. The initial decrease in NGI as the cell is charged only occurs for the first discharge indicating that this initial darkening is related to the transition from colourless solution to a yellow, polysulfide containing solution.

Although both the locations near the positive and negative electrodes show the same trend there is a slight difference in their behaviour with the positive electrode generally appearing darker at both the bottom of discharge and top of charge. To further understand the gradient of the colour change across the interelectrode space the NGI value across this

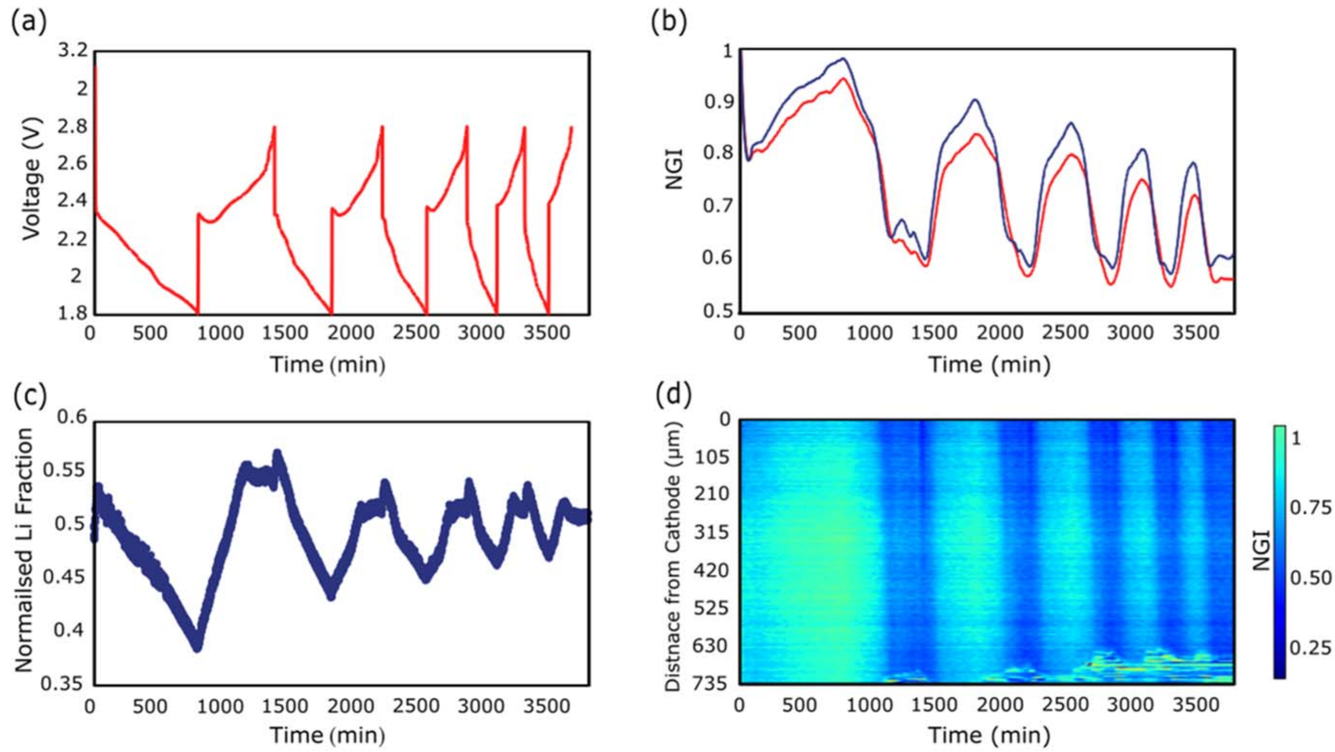

Figure 8. (a) The voltage profile of the lithium-sulfur cell cycled at 1 m Acm^{-2} across the course of the first five cycles. (b) The normalised grey intensity variation during the first five cycles at locations close to the cathode (red) and close to the anode (blue). (c) The variation of normalised lithium fraction over the course of the initial five cycles. (d) A colourmap plot showing the variation of normalised grey intensity over the course of the first five cycles in relation to the position relative to the cathode.

distance is plotted in Fig. 8d, here the *x*-axis shows time, the *y*-axis the distance from the positive electrode with the top close to the positive electrode and the bottom close to the negative electrode the NGI is represented by the colour. It should be noted that some anomalies appear close to the negative electrode at the later stages of the experiment due to dendrite formation influencing the NGI value calculations. This plot demonstrates that there is an influence on the NGI based on the distance from the cathode, the trend is however repeatable.

The normalised lithium fraction across the course of the first five cycles is shown in Fig. 8c. Again, a similar oscillating trend is observed with the lithium fraction generally decreasing during the discharge and increasing during the charge, as would be expected based on the lithium consumption and deposition predicted by the electrochemistry. Plateaus are evident at the top of charge for all cycles indicating that during this stage-of-charge where reaction is dominated by precipitation of S_8 compared to solution phased reaction, is occurring for all cycles. The lithium fraction at the top of charge appears to remain relatively constant across the course of the reaction, remaining at ca. 0.55. However, the amount of lithium consumed during each discharge decreases with each subsequent cycle, matching the decreasing capacity observed electrochemically. A slight decrease in the magnitude of the normalised lithium fraction can also be seen over multiple cycles, this is likely due to the formation of more complex, dendritic structures below the resolution of the experiment which are not captured. A similar trend is also observed at the bottom of discharge with the normalised lithium fraction gradually increasing with each cycle.

To quantify the changes occurring as the cell is cycled the NGI and normalised lithium fraction was calculated as shown in Fig. 8, along with the cells' voltage profile across this test.

The NGI is shown in Fig. 8b for two locations, one close to the cathode (red) and one close to the anode (blue). As expected, an oscillating pattern is observed that correlates to the voltage profile showing that in general as the cells is discharged the NGI increases, the electrolyte gets lighter and that as the cell is charged the NGI decreases, indicating darker electrolyte with longer chained polysulfides. The initial decrease in NGI as the cell is charged only occurs for the first discharge, indicating that this initial darkening is related to the transition from a colourless solution to a yellow polysulfide containing solution. The electrolyte gets gradually darker across the course of the five cycles, this can most likely be accounted for by an increase in polysulfide concentration in the electrolyte during cycling.

Although both the location near the cathode and near the anode show the same trend there is a slight difference in their behaviour with the cathode generally appearing darker at both the bottom of discharge and top of charge. To further understand the gradient of the colour change across the interelectrode space the NGI value across this distance is plotted in Fig. 8 (d), here the *x*-axis shows time, the *y*-axis the distance from the cathode with the top close to the cathode and the bottom close to the anode, the NGI is represented by the colour. It should be noted that some anomalies appear close to the anode at the later stages of the experiment due to dendrite formation influencing the NGI value calculations. This plot demonstrates that there is an influence on the NGI based on the distance from the cathode, the trend is however repeatable.

In order to understand the effects of areal current density on the performance of lithium sulfur batteries and its influence on the processes occurring, the experiment discussed so far was repeated with the only change being that the current density was increased from 1 mA cm^{-2} to 3 mA cm^{-2}. Figure 9 shows optical images obtained for this cell at the bottom of discharge and top of charge across the first five cycles. Figure 9a shows the capacity of the cell across these cycles. As observed for the system cycled with an areal current density of 1 mA cm^{-2} there is a relatively large difference between the charge and discharge capacities with the resulting low Coulombic efficiency suggesting irreversible reactions are occurring, this is further supported by the fact that not all of the polysulfide are converted back to S_8, as demonstrated by the fact that the colour of the electrolyte does not return to its original colourless form, indicating polysulfides are still in solution. This is similar to the observation for the cell cycled at lower current densities (see Fig. 7).

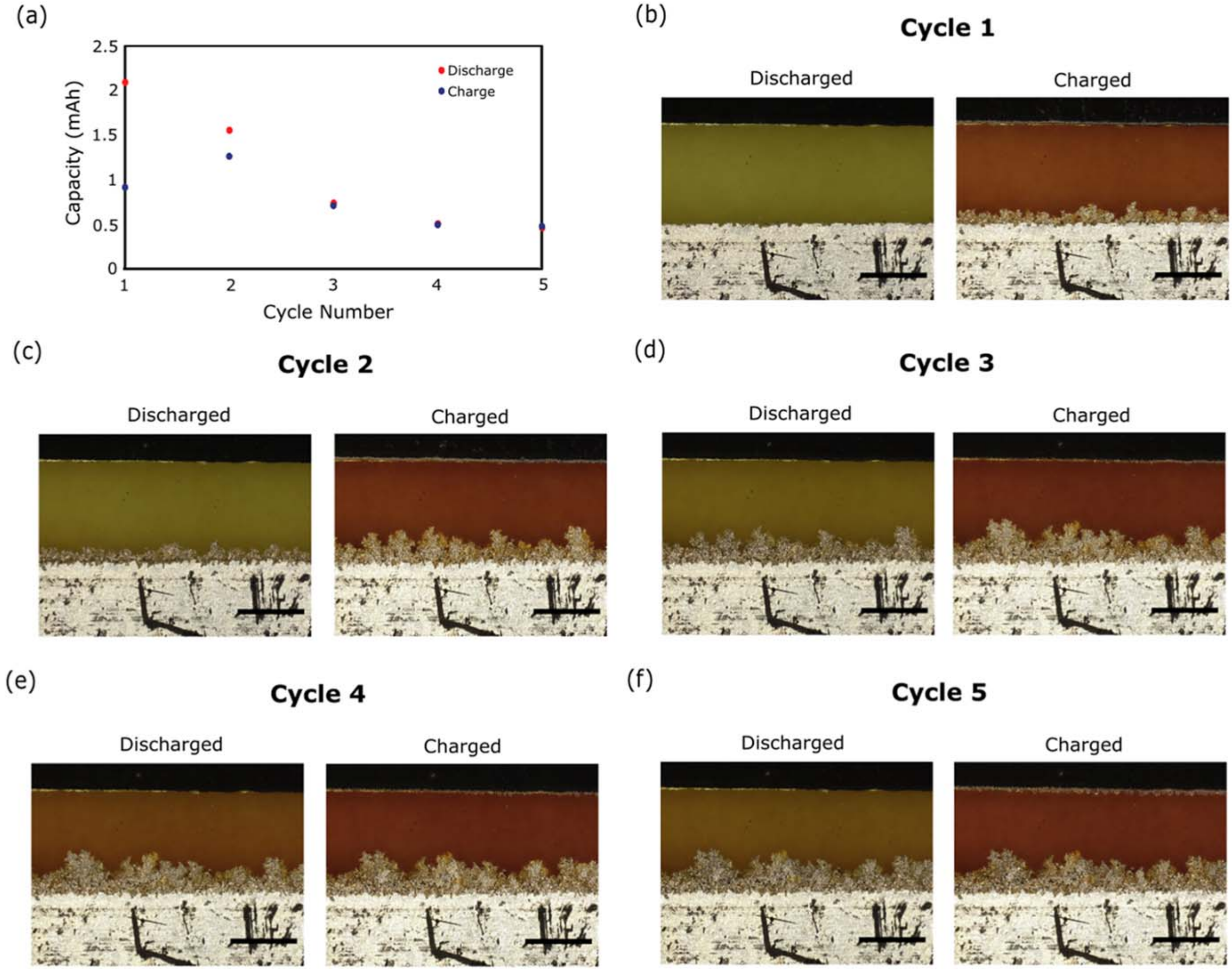

Figure 9. (a) cell capacity as a function of charge and discharge cycle when operated at 3 mA cm^{-2}. (b)-(f) Optical images showing the appearance of the bottom of discharge and top of charge for the first five cycles of the lithium-sulfur test cell. Scale bar = 500 μm.

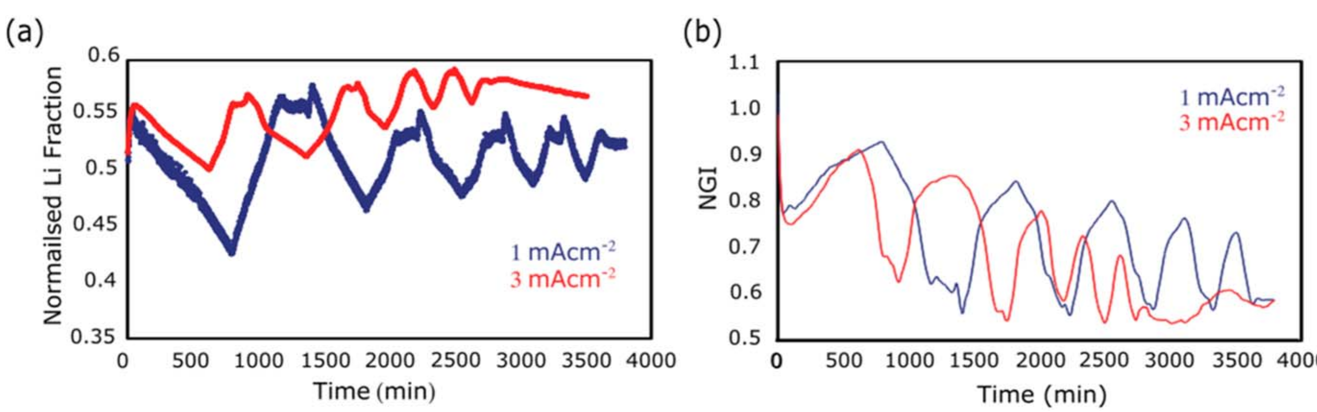

Figure 10. (a) a comparison between the variation in normalised lithium fraction for cells cycled at 1 and 3 mA cm^{-2} and the normalised grey intensity for both current densities (b).

The electrolyte for this test is again initially colourless before becoming yellow upon the dissolution of the polysulfides formed from the S_8 present in the fresh positive electrode. By the bottom of the first discharge the electrolyte is light yellow, having proceeded through a darker yellow when the longer chained polysulfides were present through to the short-chain analogues present at the bottom of discharge. Evidence of lithium stripping and consumption is also visible on the negative electrode at the bottom of the first discharge. Following the first charge the colour of the electrolyte has become much darker with the reformation of the long-chain polysulfides and significant lithium dendrite formation is observed on the negative electrode of the system.

Subsequent cycles of discharge and charge follow the same trend with the electrolyte appearing light at the bottom of discharge and

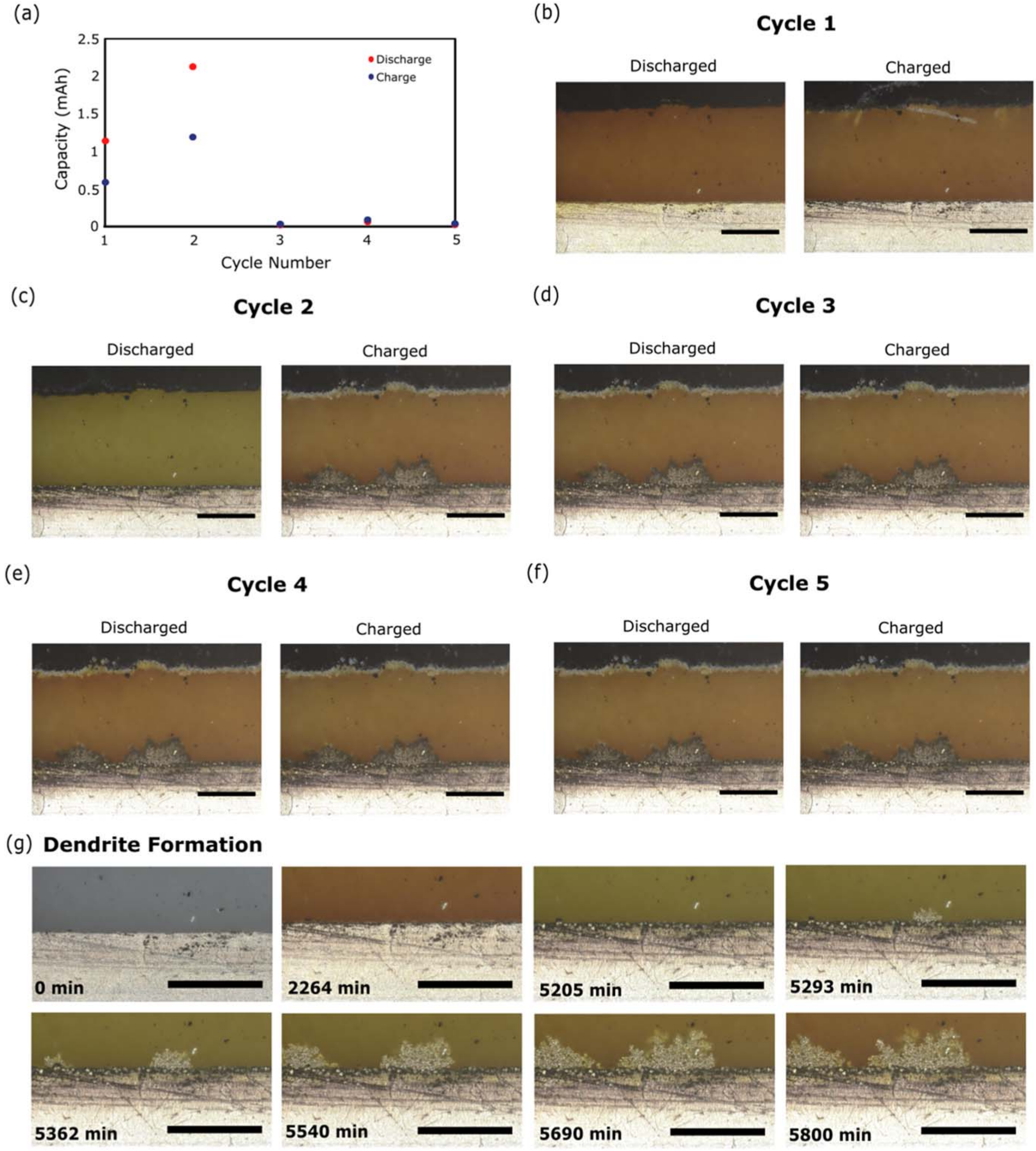

Figure 11. (a) Cell capacity as a function of charge and discharge cycle when operated at 3 μA cm^{-2}. (b)-(f) Optical images showing the appearance of the bottom of discharge and top of charge for the first five cycles of the lithium-sulfur test cell. (g) Higher magnification images showing the onset of dendrite formation during the charge of cycle 2. Scale bar = 500 μm.

darker at the top of charge. Across the course of the five cycles studied in this experiment there is an observable increase in the quantity of dendrites present at the top of each charge.

As demonstrated so far, and in accordance with previously reported literature, higher areal current densities (shown in Fig. 10) result in more significant dendrite formation and rapid degradation of the lithium-sulfur battery system. As such, a lower current density (500 mA cm^{-2}) was also investigated with the results summarised in Fig. 11. The initial discharge and charge cycles for the cell cycled at low current densities were shown to be high relative to the subsequent cycles. Initially the visual appearance of the cell is similar to that observed for previous experiments where the current density was higher. The colour change of the electrolyte was observed with darker electrolyte generally observed at the top of charge and lighter electrolyte observed at the bottom of discharge. Notably for the first two cycles of this lower current density no dendrite formation was observed on the negative electrode as would be expected for an areal current density of this value based on previously reported literature.[27]

Despite the lack of dendrite formation, some evidence of lithium consumption and deposition is observed; however, this appears to be far more uniform in nature. Following the second charge, a distinct change in the cell behaviour is observed both electrochemically and visually. At ca. 5,200 min (during the later stages of the second charge) lithium dendrite formation appears to start, as illustrated in Fig. 11g. These dendrites form and develop getting progressively worse over the course of ca. 600 min. This observed formation of the lithium dendrites at the top of the second charge correspond to a significant drop in electrochemical performance with the charge and discharge capacity of subsequent cycles dropping significantly from those observed previously.

Following the initial formation of the lithium dendrite species on the negative electrode of the cell no significant change is observed over the course of the subsequent and remaining three cycles. It should however be noted that each of these cycles are lower in capacity and corresponded to a significantly lower cycle time, which presumably contributes to the lack of development of the lithium dendrites.

The results obtained from the experiment at lower current density (750 μA cm^{-2}), summarised in Fig. 11 suggest that lower current densities do lead to a reduction in the propensity of the system to form lithium dendrites, as supported by previous literature.[27] However, as indicated in Figs. 11(c)–11((g), as soon as lithium dendrite formation begins this results in a significant and rapid degradation in the performance of the cell. This further highlights both the impact of areal current density on the performance of the cell and the importance of suppressing lithium dendrite formation in the quest to obtain lithium-sulfur cells with technologically valuable cycle lives.

Conclusions

In this paper optical microscopy is used *operando* to monitor the cycling of lithium sulfur cells and the impact of areal current density on both the performance and morphological changes occurring within the cell. Through the use of normalised grey intensities and segmentation to calculate the normalised lithium fraction we are able to quantify the changes occurring in lithium-sulfur systems moving beyond qualitative measurements and beginning to enable quantitative comparisons between systems. This paper demonstrates how the areal current density can have a significant effect on both the performance of the cell and the morphological changes that are occurring. By tracking the morphological changes that occur during cycling we are able to identify the charge limiting behaviour of this electrode formulation and track the evolution of the respective electrodes. In achieving this, we are able to closely monitor the lithium consumption and deposition, the dissolution and changes occurring in the polysulfide species, as well as track the deposition of sulfur species through the use of Raman spectroscopy, processes that are difficult to track through the majority of other available techniques.

This paper serves to demonstrate the power and potential applications for this relatively simple and cost-effective technique for tracking the processes occurring in lithium-sulfur systems. Although only the example of areal current density is demonstrated here, the implications of the effect of cell conditions, electrolyte additives, anode protections films, and cathode composition are likely able to be observed here also, again in a relatively simple and cost-effective manner.

Furthermore, the technique demonstrated in this work may support the development of broader electrochemical systems, in particular batteries which utilise conversion electrodes. The combination of visual and quantified data is a powerful tool to support the development and evaluation of electrode compositions and architectures.

Acknowledgments

The authors would like to acknowledge the Faraday Institution (Faraday.ac.uk; EP/S003053/1) for funding the energy storage work at the Advanced Propulsion Lab and Electrochemical Innovation Lab through the LiSTAR research programme (FIRG0058). The authors also acknowledge the Royal Academy of Engineering for funding the Research Chairs of Brett (including the National Physical Laboratory and HORIBA MIRA) and Shearing (CiET1718\59).

ORCID

Rhodri E. Owen https://orcid.org/0000-0002-1246-2988
Wenjia Du https://orcid.org/0000-0001-8434-4764
Paul R. Shearing https://orcid.org/0000-0002-1387-9531
Dan J. L. Brett https://orcid.org/0000-0002-8545-3126
James B. Robinson https://orcid.org/0000-0002-6509-7769

References

1. J. B. Robinson et al., "Roadmap on lithium sulfur batteries." *J. Phys.: Energy*, **3**, 031501 (2021).
2. Yelin Deng, Jianyang Li, Tonghui Li, Xianfeng Gao, and Chris Yuan, "Life cycle assessment of lithium sulfur battery for electric vehicles." *Journal of Power Sources*, **343**, 284-295 (1 March 2017).
3. Weijiang Xue, Lixiao Miao, Long Qie, Chao Wang, Sa Li, Jiulin Wang, and Ju Li, "Gravimetric and volumetric energy densities of lithium-sulfur batteries." *Current Opinion in Electrochemistry*, **6**, 92 (2017).
4. R. Purkayastha, "Degradation in lithium–sulfur batteries." *Lithium–Sulfur Batteries* (Wiley, New York)185 (2019).
5. L. Xue et al., "In Situ/Operando Raman techniques in lithium–sulfur batteries." *Small Struct.*, **3**, 2100170 (2022).
6. W. Zhu et al., "Investigation of the reaction mechanism of lithium sulfur batteries in different electrolyte systems by *in situ* Raman spectroscopy and *in situ* X-ray diffraction." *Sustain. Energy Fuels*, **1**, 737 (2017).
7. M. A. Lowe, J. Gao, and H. D. Abruña, "Mechanistic insights into operational lithium–sulfur batteries by *in situ* X-ray diffraction and absorption spectroscopy." *RSC Adv.*, **4**, 18347 (2014).
8. H. Kim et al., "*In Situ* TEM observation of electrochemical lithiation of sulfur confined within inner cylindrical pores of carbon nanotubes." *Adv. Energy Mater.*, **5**, 1501306 (2015).
9. K. Mahankali, N. K. Thangavel, and L. M. Reddy Arava, "*In Situ* electrochemical mapping of lithium–sulfur battery interfaces using AFM–SECM." *Nano Lett.*, **19**, 5229 (2019).
10. S. Risse et al., "Multidimensional operando analysis of macroscopic structure evolution in lithium sulfur cells by X-ray radiography." *Phys. Chem. Chem. Phys.*, **18**, 10630 (2016).
11. C. Tan et al., "Four-Dimensional Studies of Morphology Evolution in Lithium–Sulfur Batteries." *ACS Appl. Energy Mater.*, **1**, 5090 (2018).
12. A. Yermukhambetova et al., "Exploring 3D microstructural evolution in Li-Sulfur battery electrodes using *in situ* X-ray tomography." *Sci. Rep.*, **6**, 35291 (2016).
13. A. Vizintin et al., "The mechanism of Li2S activation in lithium-sulfur batteries: Can we avoid the polysulfide formation?" *J. Power Sources*, **344**, 208 (2017).
14. N. Saqib, G. M. Ohlhausen, and J. M. Porter, "In operando infrared spectroscopy of lithium polysulfides using a novel spectro-electrochemical cell." *J. Power Sources*, **364**, 266 (2017).
15. S. Rehman, M. Pope, S. Tao, and E. McCalla, "Evaluating the effectiveness of *in situ* characterization techniques in overcoming mechanistic limitations in lithium–sulfur batteries." *Energy Environ. Sci.*, **15**, 1423 (2022).
16. X. Lu et al., "Multiscale dynamics of charging and plating in graphite electrodes coupling operando microscopy and phase-field modelling." *Nat. Commun.*, **14**, 5127 (2023).
17. E. Kazyak et al., "Li penetration in ceramic solid electrolytes: *Operando* Microscopy analysis of morphology, propagation, and reversibility." *Matter*, **2**, 1025 (2020).
18. S. J. Banik and R. Akolkar, "Suppressing dendritic growth during Alkaline zinc electrodeposition using polyethylenimine additive." *Electrochim. Acta*, **179**, 475 (2015).
19. W. Du et al., "Observation of Zn dendrite growth via Operando digital microscopy and time-lapse tomography." *ACS Appl. Mater. Interfaces*, **15**, 14196 (2023).
20. Y-X. Song et al., "Direct tracking of the polysulfide shuttling and interfacial evolution in all-solid-state lithium–sulfur batteries: a degradation mechanism study." *Energy Environ. Sci.*, **12**, 2496 (2019).
21. D. Blanchard and M. Slagter, "In operando Raman and optical study of lithium polysulfides dissolution in lithium–sulfur cells with carrageenan binder." *J. Phys.: Energy*, **3**, 044003 (2021).
22. Y. Sun et al., "*In-operando* optical imaging of temporal and spatial distribution of polysulfides in lithium-sulfur batteries." *Nano Energy*, **11**, 579 (2015).
23. N. Otsu, "A threshold selection method from gray-level histograms." *IEEE Trans. Syst. Man Cybern.*, **9**, 62 (1979).

24. A. Sano and S. Maruyama, "Decreasing the initial irreversible capacity loss by addition of cyclic sulfate as electrolyte additives." *J. Power Sources*, **192**, 714 (2009).
25. J. J. Chen et al., "Conductive lewis base matrix to recover the missing link of Li2S8 during the sulfur redox cycle in Li–S battery." *Chem. Mater.*, **27**, 2048 (2015).
26. A. Sadezky, H. Muckenhuber, H. Grothe, R. Niessner, and U. Pöschl, "Raman microspectroscopy of soot and related carbonaceous materials: spectral analysis and structural information." *Carbon*, **43**, 1731 (2005).
27. X. Zhang, A. Wang, X. Liu, and J. Luo, "Dendrites in lithium metal anodes: suppression, regulation, and elimination." *Acc. Chem. Res.*, **52**, 3223 (2019).